Observation of linear magnetoelectric effect in the van der Waals antiferromagnets $Ni_5(TeO_3)_4X_2$ (X = Cl, Br)

Bing Yu,[1] Suyun Wang,[1] Lin Huang,[1] Yongsen Tang,[2,*] Lin Lin,[1,3,†] Guanzhong Zhou,[1] Junhu Zhang,[1] Meifeng Liu,[4] Shuhan Zheng,[4] Zhibo Yan,[1] Xiaokun Huang,[5] Junfeng Wang,[6] Jianguo Wan,[1,‡] XiangPing Jiang,[5] and Jun-Ming Liu[1]

[1]*Laboratory of Solid State Microstructures, Nanjing University, Nanjing 210093, China*

[2]*School of Science, Nanjing University of Posts and Telecommunications, Nanjing 210023, China*

[3]*Department of Applied Physics, College of Science, Nanjing Forestry University, Nanjing 210037, China*

[4]*Institute for Advanced Materials, Hubei Normal University, Huangshi 435002, China*

[5]*School of Materials Science and Engineering, Jingdezhen Ceramic Institute, Jingdezhen 333403, China*

[6]*Wuhan National High Magnetic Field Center and School of Physics, Huazhong University of Science and Technology, Wuhan 430074, China*

(Received 6 December 2023; revised 30 April 2024; accepted 4 June 2024; published 25 June 2024)

Realization of linear magnetoelectric (ME) effect in single-phase van der Waals (vdW) compounds, combined with magnetic (spin), electric dipole, and dimensions degrees of freedom, could lead to new applications, such as high-density multistate data storage. Although the linear ME effect has been broadly studied for decades, vdW materials with an intrinsic ME effect have been rarely explored so far. Using a recently proposed design principle of two-dimensional vdW materials, transition metal tellurate halides, $Ni_5(TeO_3)_4X_2$ (X = Cl, Br) with linear ME coupling, have been synthesized and remarkable ME effect is demonstrated here. The onset of simultaneous anomalies in magnetic susceptibility and specific heat suggests the noncollinear antiferromagnetic order with the Néel temperature $T_N \sim 30$ K. In addition, a clear spin-flop transition appears below T_N, driven by magnetic field along the x axis, indicating a strong magnetic anisotropy. Associated with the antiferromagnetic transition, a shape anomaly in the displacement current implies the appearance of ME response below T_N with the ME coefficient α_{xy} up to 4.2 ps/m in $Ni_5(TeO_3)_4Cl_2$. This is evidenced by the evolution of electric polarization (P_x) with magnetic field ($H//y$) along the y axis at selected temperatures. The present study suggests that $Ni_5(TeO_3)_4X_2$ is an unusual class of vdW materials hosting the linear ME behaviors, and thus an attractive platform for investigating the complicated interactions among spin order, electric polarization, and van der Waals force in layered vdW compounds.

DOI: 10.1103/PhysRevB.109.214435

I. INTRODUCTION

Linear magnetoelectric (ME) materials, in which electric polarization (P) or magnetization (M) is proportional to applied magnetic field (H) or electric field (E), have drawn a great deal of interest due to the underlying fundamental physics and promising applications in novel devices [1–5]. The inherent cross-coupling between magnetism and ferroelectricity enables emergent phenomena associated with the symmetry breaking, lattice structure, and long-range spin ordering, as exemplified by Cr_2O_3 [6], LiMPO_4 (M = Co and Ni) [7], $PbCu_3TeO_7$ [8], and $M_2Mo_3O_8$ (M: 3d transition metals) [9], among many others. Note that almost all the magnetoelectric (ME) effects are found in three-dimensional transition metal oxides, keeping in mind that dimensionality is a promising concept that generally plays a key role in determining their magnetic and electric properties [10–13]. For example, the emergence of two-dimensional (2D) ferromagnetism has stimulated strong interest in 2D ferroelectricity and multiferroicity.

Until recently, the 2D van der Waals (vdW) magnets have stood out due to their ability to offer unprecedented opportunities for low-power functional devices and interface phenomena [14–17]. Beyond that, many vdW magnets that host frustrated spin orders are expected to open up a wide range of possibilities for fundamental and applied research, e.g., multiferroics and proximate spin liquids [18,19], providing an ideal platform for exploring the ME effect in the 2D limit.

The vdW magnet $Ni_5(TeO_3)_4X_2$ (X = Cl, Br) represents a versatile class due to the presence of isostructural Ni^{2+} ($S = 1$) ions. The Ni^{2+} ions due to the three different crystalline fields, named Ni_1, Ni_2, and Ni_3, can accommodate three spin moments [20,21], as presented in Fig. 1(a). In detail, one unit cell contains three inequivalent Ni^{2+} sites, arranged in a unique configuration resembling a "claw." Here, the $[Ni_5O_{17}X_2]$ basic unit comprises two interconnected triangles with Ni_1 located in the center [20]. It is noted that the three-dimensional polar magnet Ni_3TeO_6 also hosts three inequivalent Ni^{2+} sites and presents a chiral lattice structure [22,23]. Similarly, the $[Ni_5O_{17}X_2]$ unit can be described by chiral, as shown in Fig. 1(a), while another $[Ni_5O_{17}X_2]$ unit is connected by a center inversion operation (-1) and forms a layered structure via corner sharing [20]. Then the

*Contact author: tangys@njupt.edu.cn
†Contact author: llin@njfu.edu.cn
‡Contact author: wanjg@nju.edu.cn

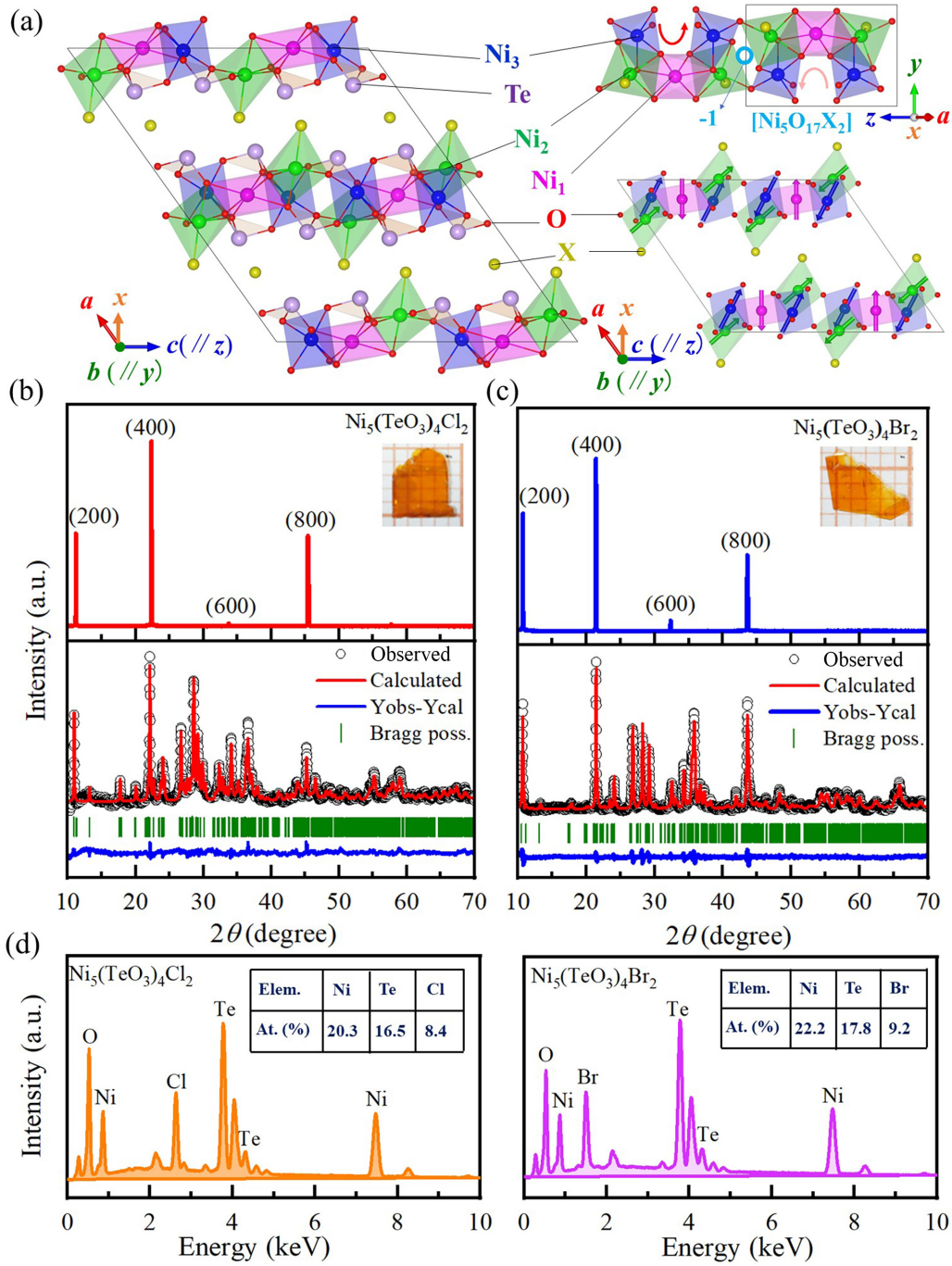

FIG. 1. (a) Schematic crystal and magnetic structures of $Ni_5(TeO_3)_4X_2$ (X = Cl, Br) with Ni^{2+} ions occupy three distinct sites, denoted as Ni_1, Ni_2, and Ni_3, respectively, and arranged in some kind of a "claw" $[Ni_5O_{17}X_2]$ basic unit. The Te^{4+}, O^{2-}, and X^- ions are also shown here. (b) The XRD patterns onto the naturally evolutive plane of [h00] directions and Rietveld refinement on the finely ground crashed crystals for (b) $Ni_5(TeO_3)_4Cl_2$ and (c) $Ni_5(TeO_3)_4Br_2$ collected at room temperature. The insets are the photo image of a typical single crystal. (d) The chemical composition analyzed with EDS.

adjacent layers of this compound are connected by vdW force. In detail, the Te^{4+} ions are located in irregular tetrahedron, and are bonded to three oxygen atoms with a bond length of 1.8–1.9 Å, while X^- ions are connected to a transition metal with a bond length of 2.4 Å, resulting in a complete-shell electronic structure. Therefore, layers are stacked with each other by vdW force. In addition to these structural features, a complex antiferromagnetic (AFM) order in $Ni_5(TeO_3)_4X_2$ is also intriguing. Especially, the Ni^{2+} moments with a lower magnetic symmetry have been found to predominantly lie in the *ac* plane, offering the possibility of intrinsic ME effect. Note that the spontaneous polarization is not available in $Ni_5(TeO_3)_4X_2$ due to the centrosymmetric $C2/c$ space group. Nevertheless, the magnetic space group of $Ni_5(TeO_3)_4X_2$ is $C2'/c$, which deserve to explore the magnetic field-induced polarization in these compounds.

In fact, the exploration of magnetically induced ferroelectric polarization along the out-of-plane in vdW magnets is generally challenging. This difficulty arises due to the presence of a van der Waals gap that separates the magnetic planes. Consequently, the superexchange paths between the layers are effectively impeded, rendering them an ideal two-dimensional system. It is one of the reasons why only a limited number of vdW magnets have been found to exhibit ME effect. Among them, the representative materials are $CuCrP_2S_6$, $NiBr_2$, $CuBr_2$, $CuCl_2$, and MI_2 (M = Mn, Co, Ni), in which the *p-d* hybridization mechanism plays a significant role in the intrinsic ME effect [24–29]. In this regard, the chiral lattice structure combined with low magnetic symmetry in bulk $Ni_5(TeO_3)_4X_2$ may give rise to a distinct ME effect, which deserves further investigation.

In this work, we have successfully grown millimeter-sized $Ni_5(TeO_3)_4X_2$ (X = Cl, Br) single crystal. Based on this advantage, we report the experimental observation of linear ME effect by combing the measurements on magnetism, specific heat, and ME effect. We found a field-driven electric polarization emerging below the Néel temperature T_N, indicative of the intrinsic ME coupling. The nondiagonal component of the linear ME coefficient, as measured under magnetic field H perpendicular to the x axis, α_{xy} reaches 4.2 ps/m in $Ni_5(TeO_3)_4Cl_2$. A symmetry analysis on the microscopic mechanism of ME effect and relevant experimental data demonstrates $Ni_5(TeO_3)_4Br_2$ and $Ni_5(TeO_3)_4Cl_2$ as new members of the 2D vdW magnets, and provides a valuable platform on ME effect in vdW magnets with chiral lattice.

II. EXPERIMENTAL DETAILS

$Ni_5(TeO_3)_4X_2$ (X = Cl, Br) single crystals were grown by the chemical vapor transport (CVT) technique using $TeCl_4$ as a transport agent [20,21]. In detail, the precursor polycrystalline samples of $Ni_5(TeO_3)_4X_2$ were obtained by using the traditional solid-phase method. First, a stoichiometric mixture of high purity NiO_2, NiX_2, and TeO_2 was thoroughly ground in the glove box. Then the mixed powder was placed in the evacuated silica ampoules, and sintered at 570 °C for 72 h in the muffle furnace. Following that, the polycrystalline powder was sealed in the quartz tube under vacuum. Then the tube was placed in a horizontal two-zone furnace, and heated at 750 °C in the change zone and 550 °C in the growth zone for 15 days, followed by furnace cooling. Large scale orange flake crystals with the size of $4 \times 4\,mm^2$ were obtained. The naturally developed plane of as-grown crystals of micrometer scale was checked using the x-ray powder diffraction (XRD; D8 ADVANCE, Bruker) in the θ-2θ mode with Cu K_α source (wavelength $\lambda = 1.5406$ Å) at room temperature. In addition, the electron dispersion spectroscope (EDS) attached to the scanning electron microscope (Quanta 200, FEI) was used to probe the chemical composition. The crystal structures presented in this paper were drawn using VESTA software [30].

Subsequently, a set of well-prepared single crystal samples were used for characterizations on magnetism, specific heat, electric polarization, and ME effect, etc. In detail, the temperature (T) dependence of dc magnetic susceptibility (χ) under the zero-field cooling (ZFC) and field cooling (FC) modes with cooling $H = 1$ kOe was measured from $T = 2$ to 300 K using the Quantum Design superconducting quantum interference device magnetometer (SQUID). Simultaneously, the magnetization (M) as a function of H at selected T was also measured. The specific heat (C_P) was measured from $T = 4$ to 60 K using the Quantum Design physical property measurement system (PPMS) in the standard procedure. In addition, the $M(H)$ data under the condition of high field were measured using the 10.5-ms short-pulse magnet in the Wuhan National High Magnetic Field Center (WHMFC).

For measuring the electric polarization (P) and ME effect, each of the flaky samples was carefully coated with silver electrodes on both the bottom and top surfaces. The P was evaluated from the standard pyroelectric current method, which is widely used to probe small electric polarization in ME coupling materials. In particular, prior to the P and ME measurements, each sample was prepared under the ME pooling fields $E \sim 200$ kV/cm along x direction and $\mu_0 H = 9$ T in the $\boldsymbol{E}$ ($//x$)$\perp \boldsymbol{H}$ (or $//\boldsymbol{H}$) arrangements during the cooling down to selected T. Then the poling fields were removed, and the sample was short-circuited for about one hour and submitted to a slow warming process at a fixed heating rate of 4 K/min from 2 to 35 K under the selected H. Moreover, the ME current ΔI_x and field-induced polarization (ΔP_x) along the x axis (labeled as $y//[0k0]$, $z//[00l]$, $x\perp yz$) were measured under selected T with $H(//y)$ ramping from $+H \rightarrow -H \rightarrow +H$ at a rate of 100 Oe/s using the same ME poling procedure. The current released from the sample was collected using the Keithley 6514 electrometer connected to the PPMS. The field-driven P can be obtained by performing the integration of current with respect to time.

Spin-polarized density functional theory (DFT) calculations were performed with the plane-wave code VASP [31] using the projector-augmented wave method [32]. The exchange and correlation effects were described within the generalized gradient approximation with Perdew-Burke-Ernzerhof parametrization [33]. A cutoff energy of 520 eV was adopted for the plane-wave expansion of the electronic wave function. The density of K points in real space was less than $0.04 \times 0.04 \times 0.04$ Å^{-3} for all calculations, based on the Γ-center method. The lattice constant was fixed as the experimental data, and all atoms were fully relaxed, with residual forces < 0.02 eV/Å per atom and the electron energy convergence criteria of 1×10^{-6} eV. A noncollinear GGA + U calculation was implemented with the parameters as 5.0 eV or Ni element [34].

III. RESULTS AND DISCUSSION

A. Crystal structure

The naturally grown $Ni_5(TeO_3)_4X_2$ (X = Cl, Br) single crystals exhibit transparent and flaky morphology, as shown in the insets of Figs. 1(b) and 1(c), where the room temperature slow-scan XRD pattern onto the naturally developed plane is presented. One can see that the very sharp diffraction peaks are well indexed by the (h00) direction of the standard Bragg spectrum. In addition, to further check the crystal structure, we have crushed some selected single crystal samples into powder. Then the obtained powder was checked by the XRD. The refined structure of $Ni_5(TeO_3)_4X_2$ fits the

TABLE I. Structural parameters for $Ni_5(TeO_3)_4Cl_2$ and $Ni_5(TeO_3)_4Br_2$ refined from XRD of crushed crystals at room temperature.

Sample	a (Å)	b (Å)	c (Å)	α (°)	β(°)	γ (°)
$Ni_5(TeO_3)_4Cl_2$	19.61284	5.23841	16.30349	90.000	90.000	125.378
$Ni_5(TeO_3)_4Br_2$	20.31899	5.2434	16.32544	90.000	90.000	125.075
	Atom	Wyckoff	x	y	z	
	Ni1	8f	0.00830	0.19100	0.61990	
	Ni2	8f	0.09623	0.22860	0.48674	
	Ni3	4e	0.00000	0.25554	1/4	
	Te1	8f	0.12496	0.32054	0.13196	
$Ni_5(TeO_3)_4Cl_2$	Te2	8f	0.13860	0.28546	0.87389	
	Cl	8f	0.24808	0.18643	0.59794	
	O1	8f	−0.03690	0.26068	0.10807	
	O2	8f	0.10597	0.20364	0.52451	
	O3	8f	0.08493	0.35942	0.59111	
	O4	8f	0.11491	0.05480	0.79903	
	O5	8f	0.16890	−3/8	0.08820	
	O6	8f	0.12393	0.08567	0.77011	
	Ni1	8f	0.99340	0.77124	0.40215	
	Ni2	8f	0.08759	0.21745	0.47727	
	Ni3	4e	0.00000	0.76010	3/4	
	Te1	8f	0.87852	0.30500	0.36544	
	Te2	8f	0.14093	0.70483	0.37728	
$Ni_5(TeO_3)_4Br_2$	Br	8f	0.26134	0.81990	0.89917	
	O1	8f	0.09277	0.77238	0.52239	
	O2	8f	0.39898	0.79673	0.89234	
	O3	8f	0.09529	1.26866	0.36262	
	O4	8f	0.88752	0.71086	0.25229	
	O5	8f	0.00103	0.73095	0.89101	
	O6	8f	0.84287	0.23252	0.25025	

$Ni_5(TeO_3)_4Cl_2$: $R_{wp} = 2.83$, $\chi^2 = 1.91$; $Ni_5(TeO_3)_4Br_2$: $R_{wp} = 3.09$, $\chi^2 = 2.17$

centrosymmetric $C2/c$ space group with unit cell parameters $a = 19.61284$ Å, $b = 5.23841$ Å, $c = 16.30349$ Å, $\alpha = \gamma = 90°$, and $\beta = 125.378°$ for $Ni_5(TeO_3)_4Cl_2$, and $a = 20.31899$ Å, $b = 5.24340$ Å, $c = 16.32544$ Å, $\alpha = \gamma = 90.000°$, and $\beta = 125.073°$ for $Ni_5(TeO_3)_4Br_2$, in agreement with previous reports [20,21], as shown in Figs. 1(b) and 1(c). More detailed refined structure parameters for $Ni_5(TeO_3)_4Cl_2$ and $Ni_5(TeO_3)_4Br_2$ can be found in Table I. Furthermore, the obtained $Ni_5(TeO_3)_4X_2$ single crystals were checked for their chemical composition mapped using the electron dispersion spectroscopy (EDS) technique. A uniform distribution of Ni, Te, and Cl (Br) elements were obtained. In Fig. 1(d), we plot the EDS spectra of $Ni_5(TeO_3)_4Cl_2$ and $Ni_5(TeO_3)_4Br_2$, and the Ni:Te:Cl (Br) ratio for these crystals is quite close to the nominal ratio 5:4:2. All above results obtained by us imply the good quality of these crystals, sufficient for the following characterizations on magnetic properties, specific heat, electric polarization and ME effect.

B. Magnetic susceptibility and specific heat

Figures 2(a) and 2(b) show the measured $\chi(T)$ data under $\mu_0 H = 0.1$ T (FC mode) applied along the x, y and z axes for $Ni_5(TeO_3)_4Cl_2$ and $Ni_5(TeO_3)_4Br_2$, respectively, where $y//b$ axis, $z//c$ axis, and $x \perp yz$ plane. Overall, the two compounds exhibit similar magnetic behaviors, suggesting that they host similar magnetic structure. Here, we take $Ni_5(TeO_3)_4Cl_2$ as an example to highlight the characteristics below. First, by fitting the high-T data ($T > 200$ K) of $\chi(T)$ using the Curie-Weiss law, one obtains the Curie-Weiss temperature $\theta_{CW} \sim -52$ K [−39 K for $Ni_5(TeO_3)_4Br_2$] and an effective moment of $2.2\mu_B$/Ni, which implies the non-negligible contribution of the orbital angular momentum. Second, upon further decreasing T, a broad peak appears at around $T_{N1} \sim 30$ K for the cases of $\chi_x(T)$ and $\chi_z(T)$, followed by a clear anomaly at $T_{N2} \sim 22.5$ K. These anomalies are in accord with a previous report [21]. The $\chi_y(T)$ curve shows an evident difference from the curves along the other two directions, suggesting a strong easy-plane anisotropy. Third, the anomaly at T_{N1} indicates the onset of AFM order, while the broad peak above T_{N1} is indicative of the development of short-range correlation. In addition, the anomaly at T_{N2} may result from the temperature dependence of the Ni1 moment being different from those of Ni2 and Ni3 based on the single crystal neutron diffraction in $Ni_5(TeO_3)_4Br_2$ [20]. It is worth noting that the magnetic behaviors can be attributed to the two-dimensional Ni^{2+} zigzag layers separated by nonmagnetic Te and Cl layers. Moreover, the $\chi_y(T)$ data show a continuous increase with decreasing, but tend to be saturated at the lowest measured $T \sim 2$ K, suggesting that the magnetic structure may not be of a simple collinear AFM order under the region of low T.

The Tdependent C_P data for $Ni_5(TeO_3)_4Cl_2$ and $Ni_5(TeO_3)_4Br_2$ are presented in Figs. 2(c) and 2(d), respectively. One can find a λ-type peak at T_{N1}, indicating

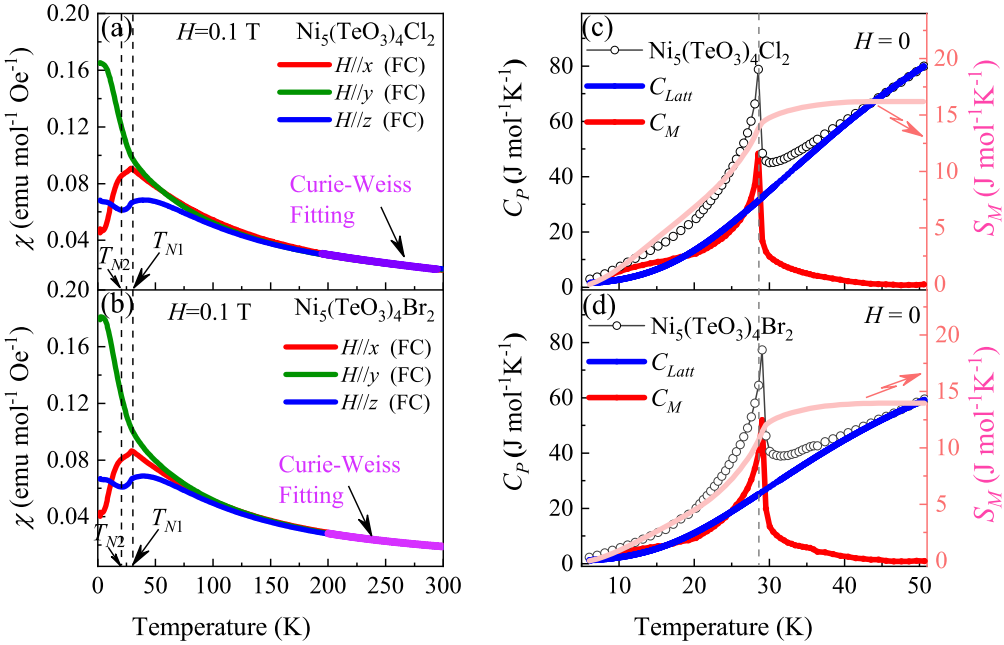

FIG. 2. (a),(b) The dc magnetic susceptibilities χ of $Ni_5(TeO_3)_4X_2$ as a function of temperature in the sample's geometry aligned along $y//[0k0]$, $z//[00l]$, and $x\perp yz$ plane with a measuring field of 0.1 T. The light purple curves represent data obtained using the Curie-Wiess fitting under $T > 200$ K. (c), (d) The specific heat variations of $Ni_5(TeO_3)_4X_2$ at zero field with magnetic contribution C_M. The T dependence of magnetic entropy $\Delta S_M(T)$ is also plotted.

a second-order AFM transition. Here, the Debye model is used to fit the $C_p(T)$ data between $T = 2$ and 50 K to evaluate the photonic contribution. After subtracting the photonic contribution (C_{Latt}), the magnetic contribution C_M can be obtained, as shown in the red solid lines. Because the obtained C_{Latt} from the Debye model is much smaller than that deduced from the mean-field theory, it shows a large magnetic contribution ($\sim$50 J mol^{-1} K^{-1}) at the AFM transition compared with the value of 33.2 J mol^{-1} K^{-1} deduced from the mean-field theory. Such difference implies the presence of short-range magnetic interaction above T_{N1} in $Ni_5(TeO_3)_4X_2$ [35]. Moreover, we plot the T dependence of magnetic entropy $S_M(T)$ of $Ni_5(TeO_3)_4Cl_2$ and $Ni_5(TeO_3)_4Br_2$ in the right axis of Figs. 2(c) and 2(d). It shows that S_M reaches up to 11 J mol^{-1} K^{-1} at T_{N1}, and saturates near 50 K with saturation value of 15 J mol^{-1} K^{-1}, which is almost half of the theoretically predicted value ($5R\ln 2 \sim 28.8$ J mol^{-1} K^{-1}). The result is similar to recently reported values for other magnetic materials [36].

While the two compounds show quite similar $\chi(T)$ and $C_P(T)$ behaviors, one is allowed to claim that they may adopt a similar magnetic structure. We use first-principles calculations to demonstrate the magnetic structures of $Ni_5(TeO_3)_4Cl_2$ and $Ni_5(TeO_3)_4Br_2$. Our calculation results reveal that both $Ni_5(TeO_3)_4Cl_2$ and $Ni_5(TeO_3)_4Br_2$ share the same magnetic point group $C2'/c$, noting that a slight tilting of moments may exist in $Ni_5(TeO_3)_4Cl_2$ compared to $Ni_5(TeO_3)_4Br_2$, as show in Figs. 3(a) and 3(b). In additional, Figs. 3(c) and 3(d) present the polar plots of the calculated magnetic anisotropy energy (MAE) vs rotation angle in the xz, xy, and yz planes for the two compounds, respectively, noting that xz represents the angle from the x axis in the xz plane. The MAE of $Ni_5(TeO_3)_4Cl_2$ in xy and yz planes is 0.2 meV/Ni and 0.19 meV/Ni, respectively, implying a hard axis along the y direction. In contrast, $Ni_5(TeO_3)_4Br_2$ exhibits a stronger MAE, probably attributed to the weak spin-orbit coupling in $Ni_5(TeO_3)_4Cl_2$, taking CrX_3 (X = Cl, Br) as reference [37]. It is evident that the hard axis of $Ni_5(TeO_3)_4Cl_2$ also aligns with the y direction, while the easy plane is confined to the xz plane, similar to the case of $Ni_5(TeO_3)_4Br_2$.

C. Low-field and high-field magnetization

Subsequently, the H-dependent $M(H)$ in the $H//x$ and $H//y$ geometry, named M_x and M_y, are presented in Figs. 4(a)–4(d) for $Ni_5(TeO_3)_4Cl_2$ and $Ni_5(TeO_3)_4Br_2$, respectively. At low field, M_x increases linearly with H. However, as H continues to increase, M_x gradually deviates from linearity and shows rapid enhancement to $\mu_0 H = 9$ T. Unfortunately, no clear metamagnetic transition has been observed yet. In contrast, the M_y and M_z increase almost monotonically with H, as seen in Figs. 4(c) and 4(d).

In order to further check any possible transition, we performed high magnetic field measurements in $Ni_5(TeO_3)_4Cl_2$ up to 50 T in the $H//x$, $H//y$, and $H//z$ geometries, at $T = 4.2$ K, as shown in Fig. 4(e). Obviously, there is a rapid upturn of M_x taking place at approximately a critical field $H_{\text{SF}} \sim 11$ T, evidenced by the peak of $d\,M_x/dH$ shown in Fig. 4(f). While previous neutron powder diffraction revealed that the Ni^{2+} moments were ordered with the major component along the [101] diagonal, as illustrated in Fig. 1(a), we can attribute the change of magnetization to the spin-flop transition. Then M_x increases quasilinearly with increasing H, and no metamagnetic transitions for M_y and M_z are observed upon H increasing to 50 T, indicating robust AFM interaction among the Ni^{2+} moments on the xz plane. In addition, compared with

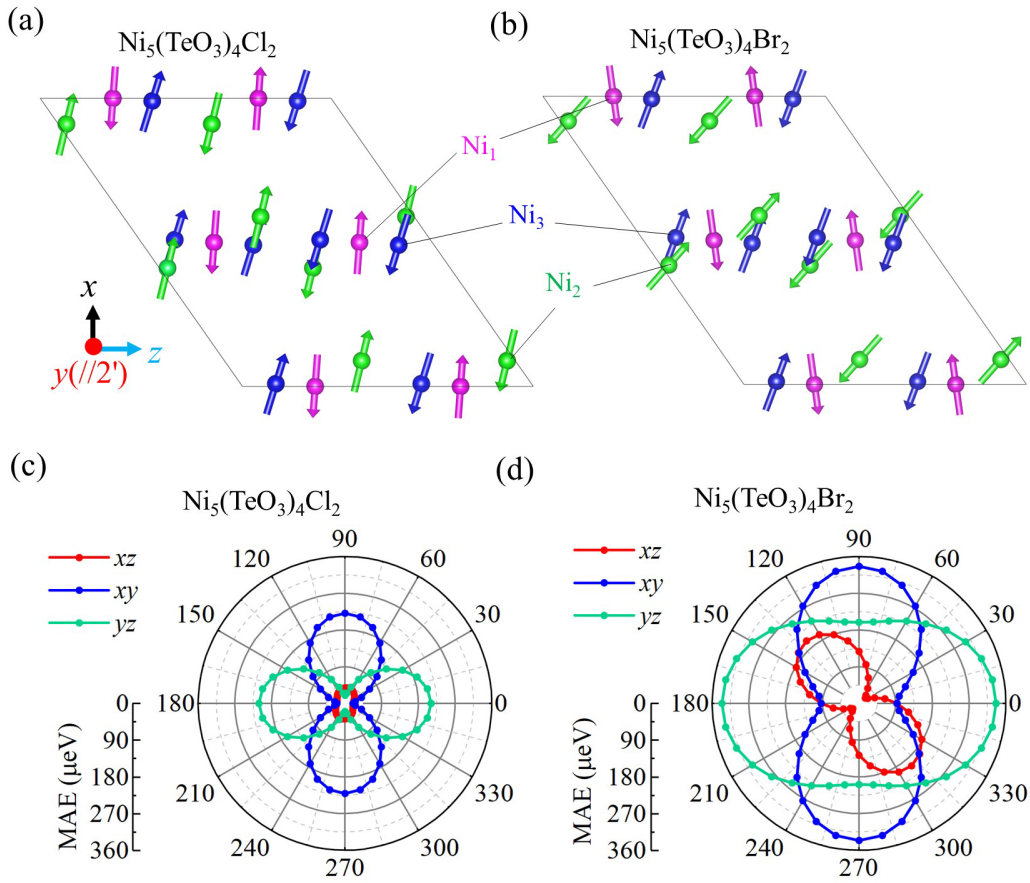

FIG. 3. (a),(b) The schematic Ni^{2+} magnetic structures at the ground AFM state by first-principles calculations for $Ni_5(TeO_3)_4Cl_2$ and $Ni_5(TeO_3)_4Br_2$. (c),(d) Calculated magnetic anisotropy energy (MAE) in $Ni_5(TeO_3)_4Cl_2$ and $Ni_5(TeO_3)_4Br_2$, respectively.

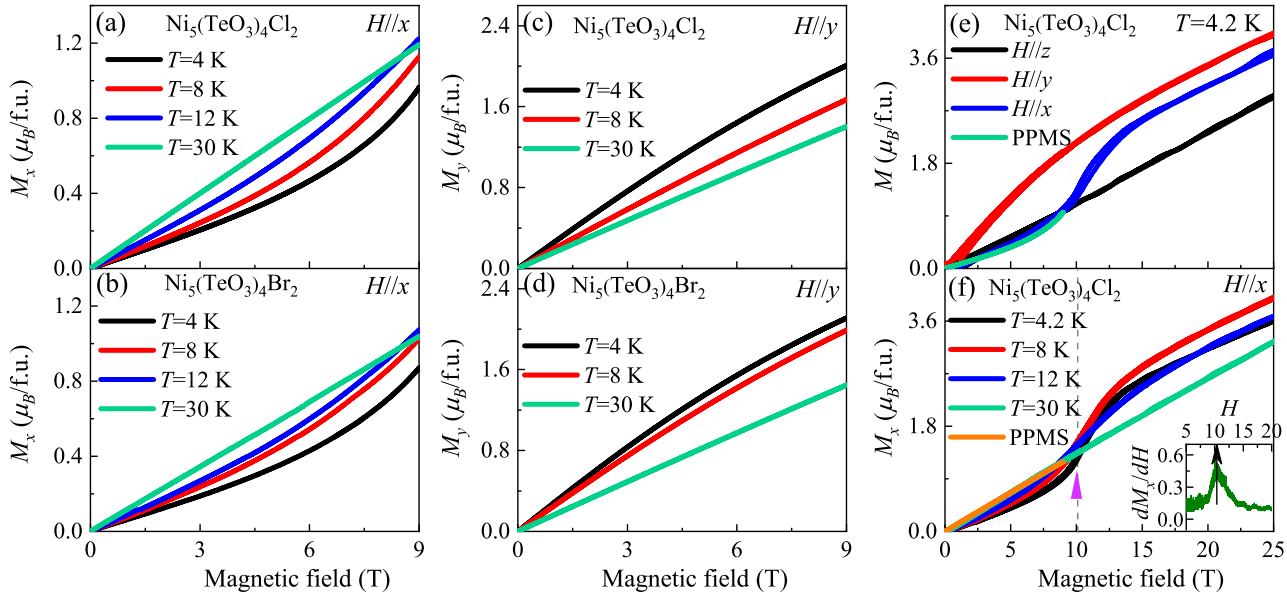

FIG. 4. The H dependence of magnetization M at selected temperatures with fields applied along (a), (b) $H//x$, (c), (d) $H//y$, in $Ni_5(TeO_3)_4Cl_2$ and $Ni_5(TeO_3)_4Br_2$, respectively. (e) M along three directions with H up to 25 T at $T = 4.2$ K for $Ni_5(TeO_3)_4Cl_2$. (f) M_x under the selected temperatures with H up to 25 T for $Ni_5(TeO_3)_4Cl_2$.

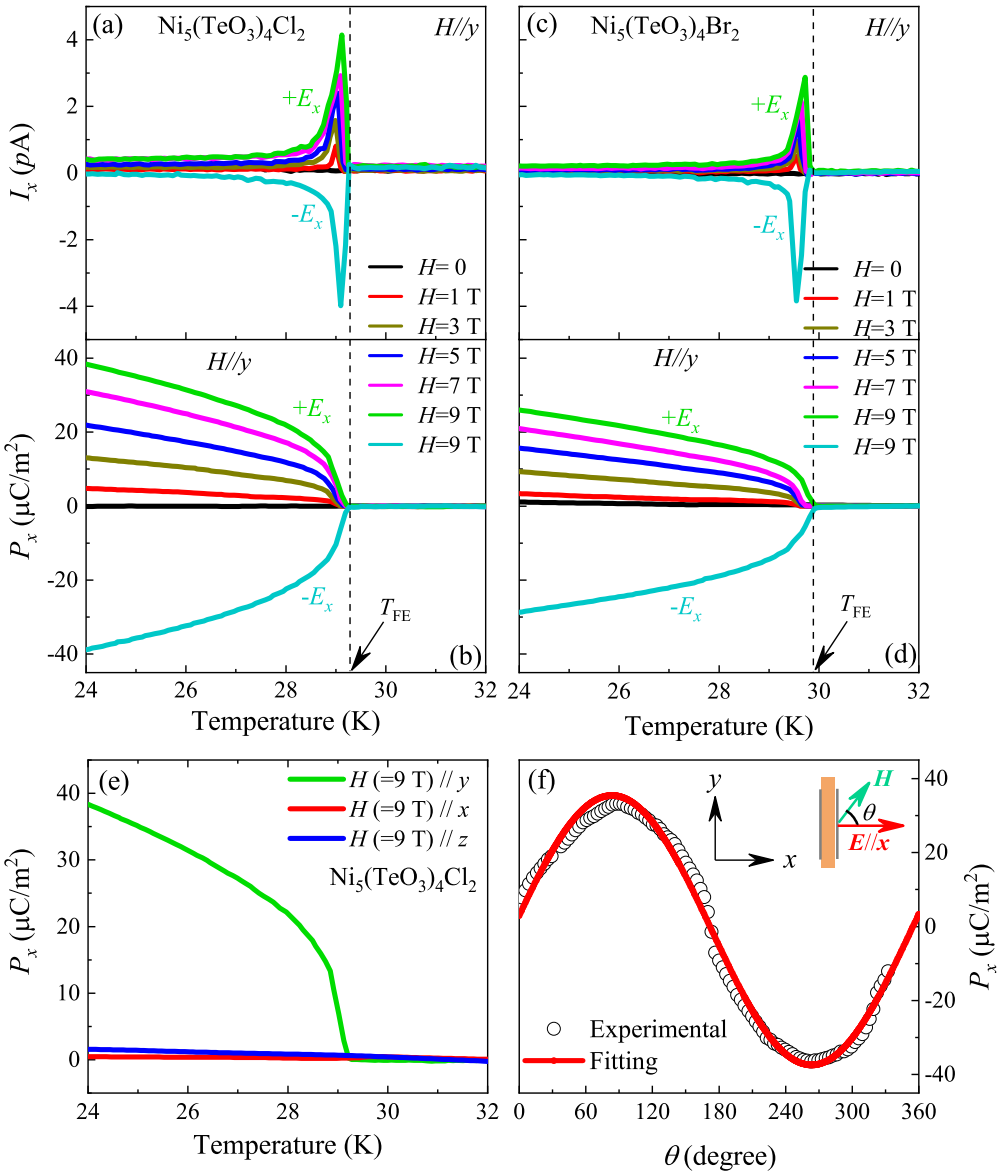

FIG. 5. The temperature dependence of (a), (c) pyroelectric current $I_x(T)$, (b), (d) electric polarization P_x with various magnetic fields up to 9 T applied along $H//y$ in $Ni_5(TeO_3)_4Cl_2$ and $Ni_5(TeO_3)_4Br_2$, respectively. (e) The temperature profiles of polarization P_x at magnetic fields $H = 9$ T along the x, y, and z directions for $Ni_5(TeO_3)_4Cl_2$. (f) The experimental and theoretical results of θ dependence of P_x. The schematic experimental configuration is plotted in the inset.

the saturation moment $M_{sat} = 10\mu_B$/f.u., the magnetizations along the three directions are far from saturated, assuming that all the Ni^{2+} ions are in the high-spin ($S = 1$) state. To this end, the low-field and high-field magnetizations reveal the metamagnetic transition behaviors, which allow us to explore the field-driven electric polarization and ME effect in the vdW $Ni_5(TeO_3)_4X_2$ single crystals.

D. Field-induced electric polarization and ME response

It is important to note that the spontaneous polarization is not available in $Ni_5(TeO_3)_4X_2$ due to the centrosymmetric $C2/c$ space group. However, this statement does not rule out the possibility of a linear ME response in certain frustrated magnets with unique spin structures, noting that the magnetic space group $Ni_5(TeO_3)_4X_2$ is $C2'/c$, which allows us to investigate the ME coupling effect in these compounds. In addition, we note that our naturally grown crystals are basically flakes with diameter of ~4 mm and thickness of 1–100 μm, as shown in the inset of Figs. 1(b) and 1(c). Therefore, only the field-driven electric polarization and ME effect along the x direction will be discussed below. Of course, the ME tensors also allow field-induced polarization along the y and z directions, which unfortunately are not accessible in this work.

Figures 5(a)–5(d) show the pyroelectric current (I_x) and electric polarization (P_x) for H parallel to y (or b) axis for $Ni_5(TeO_3)_4Cl_2$ and $Ni_5(TeO_3)_4Br_2$, respectively. Overall, two compounds exhibit similar electric behaviors. In detail, under the absence of magnetic field, no electric polarization was observed, consistent with the symmetry requirement of nonpolar $C2/c$ space group. Once magnetic field H_y is applied, the $I_x(T)$ data present a rapid rise only around the AFM ordering at

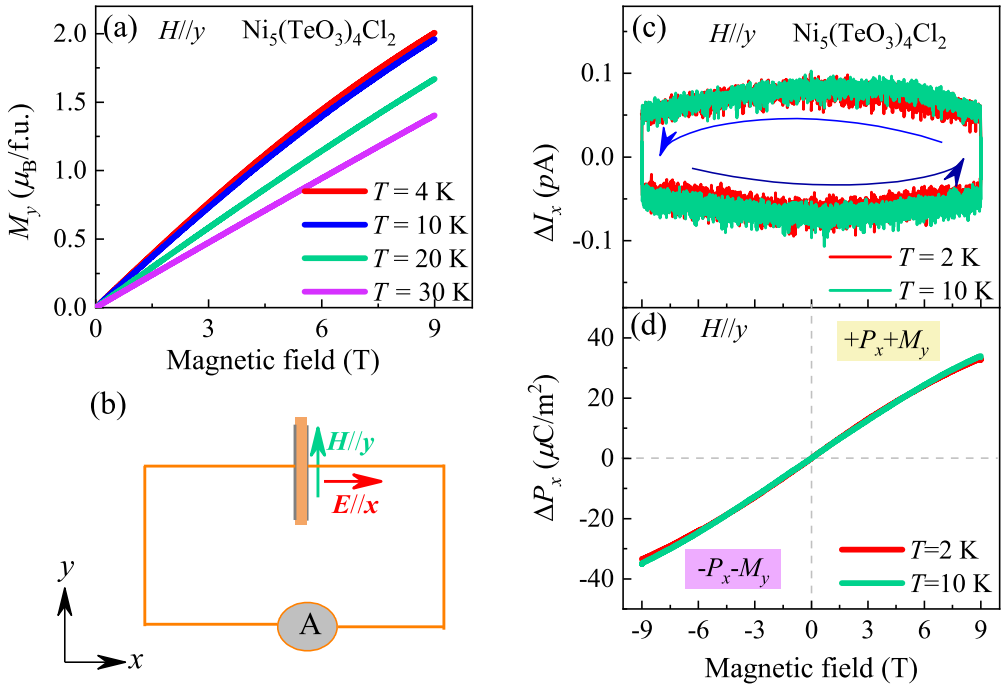

FIG. 6. The H dependence of M_y (a), ME current ΔI_x (c), and ΔP_x (d), under H along y direction under selected T, respectively. The schematic experimental configuration is plotted in (b).

T_{N1}, and forms distinct peaks at nonzero H. The occurrence of field-induced polarization and AFM ordering at T_{N1} indicates an intrinsic coupling between the magnetism and the field-driven ferroelectricity.

The intensity of P_x is proportional to the applied magnetic field, and reaches up to ~40 μC/m^2 under $H \sim 9$ T. In contrast, $Ni_5(TeO_3)_4Br_2$ exhibits relatively weak ME effect. Besides, the $I_x(T)$ is symmetrical under positive and negative poling electric field, indicating that the polarization can be switched by reversing E. Furthermore, we also probed the T dependence of I_x for $H//x$ and $H//z$ configurations at $\mu_0 H = 9$ T, as illustrated in Fig. 5(e). Apparently, there is no magnetically induced polarization for $H//x$, while for the case of $H//z$, a very small polarization is retained, which should be attributed to the slight tilt of the sample rather than intrinsic signals.

In order to investigate more details in the ME effect, in Fig. 5(f) we present the measured P_x for $Ni_5(TeO_3)_4Cl_2$ along the x axis as a function of the angle θ of $H = 9$ T, with respect to the x axis, at $T = 4$ K. Intriguingly, a periodic variation of P_x upon the H rotation was observed. The polarization decreases from 38 μC/m^2 at $\theta = 90°$ and changes its sign from positive to negative at $\theta = 180°$, and then switches to -38 μC/m^2 at $\theta = 270°$, whereas H is antiparallel to the y axis. This indicates that the polarization can be reversed by rotating H. The maximum P_x is consistent with the data shown in Fig. 5(b). Furthermore, the periodic variation of $P_x(H)$ is well fitted by the term $(\sin\theta)$ upon the rotation of H from the x axis to the y axis, exhibiting a strong anisotropy in the magnetically induced polarization with H along the x axis ($\theta = 0$) and y axis ($\theta = 90°$), respectively.

Here, for reference, we plot again the $M_y(H)$ curves at selected T, as shown in Fig. 6(a). To further examine the ME effect, we performed more detailed measurements on the ME current (ΔI_x) and H-induced polarization (ΔP_x) against H_y upon H ramping from +9 T → −9 T → +9 T at a rate of 100 Oe/s, for $Ni_5(TeO_3)_4Cl_2$, as illustrated in Fig. 6(b). Figures 6(c) and 6(d) exhibit the field-induced ΔI_x and ΔP_x as a function of H_y at $T = 2$ K and $T = 10$ K, respectively. More intuitive linear ME effects are unambiguously presented.

Here, several features of the ME response should be highlighted. First, the ME coefficient defined by $\alpha_{xy} = dP/dH = 4.2$ ps/m is obtained according to our experimental results, as shown in Fig. 6(d). This result is considerably larger than that observed in the case of $CuCrP_2S_6$ [18], making $Ni_5(TeO_3)_4Cl_2$ a promising candidate for high-performance ME coupling materials among the vdW magnets. Second, the observed ME behaviors here are indeed similar to the cases of Cr_2O_3, $A_4Nb_2O_9$ (A = Fe, Mn, Ni, Co) [6,38,39], but different from the cases of $LiCoPO_4$ and $CoSe_2O_5$, where the ME current changes its sign once the magnetic field flips from positive to negative values [7,40]. As shown in the inset of Fig. 6(d), the independent ferroic quantities P_x and M_y are perpendicular to each other, namely ($+P_x$, $+M_y$) and ($-P_x$, $-M_y$) states are obtained. To the best of our knowledge, the discrepancy of ME behaviors in these ME compounds is caused by the ME domains, which are selected by the pooling fields [41,42]. It is worth noting that the existence of off-diagonal components may imply the occurrence of the ferrotoroidal order ($\boldsymbol{T}_z = \boldsymbol{r}_x \times \boldsymbol{S}_y$) in $Ni_5(TeO_3)_4X_2$ [43]. As shown in Figs. 7(a) and 7(b), the noncollinear antiferromagnet ordering results from $Ni_m^{2+}(m = 1, 2, 3)$ sites in three different crystal fields. Under $H//y$, the moment of the Ni_m^{2+} ions cants toward the direction of the magnetic field, which breaks the $2'$ symmetry and allows electric polarization along the x and z directions. In this case, the polarization P_x (or P_z) can be induced orthogonal to the magnetic field $H//y$. As a consequence, a ferrotoroidic state is established, in which the

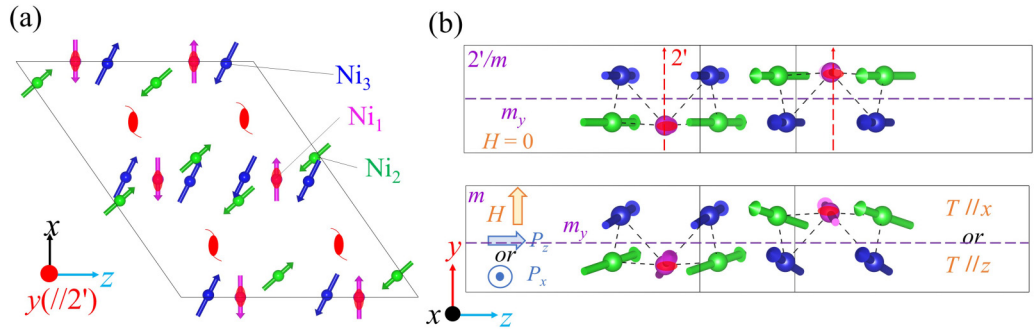

FIG. 7. (a) The schematic Ni^{2+} magnetic structure at the ground AFM state. (b) Schematic diagram between the toroidal moment and induced P with external magnetic field $H//y$. The symbols in (a) and (b) represent the symmetric operation, including twofold rotation operation along y direction and mirror operation lying in the $y/2$ plane.

toroidal moment T aligns along the z or x axis, as shown in Fig. 7(b). Of course, these call for future investigations.

E. Discussion

Given the aforementioned unique ME effect in vdW antiferromagnet $Ni_5(TeO_3)_4X_2$ (X = Cl, Br), it is important to discuss the microscopic mechanism of the ME coupling. First, one believes that the ferroelectricity in $Ni_5(TeO_3)_4X_2$ is generated by the magnetic field-driven spin ordering of Ni^{2+}. We then focus our attention on the magnetic structure variation to better understand the ME mechanism. For a better illustration of the magnetic structure, we plot the spins in Fig. 7(a) and 7(b) with the Cartesian coordinates defined as, $\boldsymbol{y}//[0k0]$, $\boldsymbol{z}//[00l]$, and $\boldsymbol{x}\perp\boldsymbol{y}z$ plane, respectively. From the viewpoint of tensor analysis, according to Neuman's principle, linear ME tensor α_{ij} for this AFM ground state can be given as [44]

$$\alpha_{ij} = \begin{pmatrix} 0 & \alpha_{xy} & 0 \\ \alpha_{yx} & 0 & \alpha_{yz} \\ 0 & \alpha_{zy} & 0 \end{pmatrix}, \tag{1}$$

under $H < H_{SF}$. One can see that the ME coefficients α_{yx}, α_{xy}, α_{zy}, and α_{yz} are nonzero, while the polarization along the y and z directions are difficult to obtain owing to the size of single crystals. Fortunately, the field-induced polarization along the x ($//E$) direction $P_x = \alpha_{xy}H_y$ can be obtained, consistent with our result as presented in Figs. 5 and 6.

Figures 7(a) and 7(b) uncover the twofold rotation operation. Considering the time inversion symmetric operation, the operation is expressed as $2'(//y)$. Moreover, a glide operation along the z direction, as plotted in Fig. 7(b), produces a mirror plane $m_y(\perp y)$, which lies in the $y/2$ plane. Obviously, under $H = 0$, the Ni^{2+} moments located on the xz plane with a propagation vector $\boldsymbol{q} = (q_1, 0, q_2)$ does not break the symmetry of the $2'$ symmetry. Thus, the electric polarization is zero in the absence of magnetic field. Second, applying the magnetic field H (below H_{SF}) along y direction gives rise to the breaking of the $2'$ symmetry which leads to a transformation of the magnetic point group into m_y, allowing electric polarization along the x and z directions, which is consistent with the nonzero ME coefficients α_{yx} and α_{zy}, as show in Fig. 7(b). All these discussions fit well with our experimental results. In addition, it is known that these off-diagonal components can give rise to nonreciprocal optical responses such as nonreciprocal linear dichroism and directional dichroism. For example, we can know that the direction of the toroidal moment not only lies in the layer ($\tau_z = p_x \times m_y$), but also is along the x direction ($\tau_x = p_y \times m_z$), due to the ME coefficient being also nonzero for the present material. Hence, the nonreciprocal optical effect could appear in the direction of light to be parallel to the x axis. Therefore, further investigation is highly desired to explore these effects [45].

Now, we turn to briefly discuss the magnetically induced polarization from a microscopic perspective. Starting from the perspective that the full Hamiltonian of magnetic systems was regulated by the electric field, the traditional magnetic linear magnetoelectric coupling mechanisms are single-ion anisotropy, symmetric superexchange, antisymmetric superexchange, dipolar interactions, and Zeeman energy [46–48]. Considering the three sublattices of Ni moments and noncollinear spin ordering, while also taking into account the four interactions mentioned above [20], i.e., single-ion anisotropy, symmetric superexchange, antisymmetric superexchange, and Zeeman energy, it is quite a challenge to accurately handle the spin Hamiltonian. However, the previous neutron data also revealed that the DM interaction, leading to a noncollinear spin ordering, and single-ion anisotropy arising from different crystal fields, are non-negligible in the system [20]. Hence, to some extent, single-ion anisotropy and antisymmetric exchange interaction should play a significant role in the origin of ME in $Ni_5(TeO_3)_4X_2$.

In addition, it is noted that the linear ME coupling effect and multiferroicity originate from the same microscopic origin and can be described in a unified way [49]. Here, we are in a position to discuss the possible microscopic mechanism for the ME effect in $Ni_5(TeO_3)_4X_2$, based on the spin current [50], exchange striction [51], and p-d hybridization mechanisms [52]. By knowing the noncollinear antiferromagnet orders of Ni^{2+}, which host three sublattices with different magnitudes and directions, the spin current mechanisms deserve to be discussed first. It is believed that the moments are in the xz plane forming a cycloid with $h = S_i \times S_j$ along the y direction. Then for $\boldsymbol{q}$ along the x (or z) direction, the spin current mechanism gives a local polarization P_z (or P_x) $= h \times q$ along the z (or x) direction, as observed in Figs. 5 and 6, while the p-d hybridization mechanism is closely associated with the directions of the single magnetic ion and coordination ions. This issue extends beyond the scope of the current category

discussion as theoretical calculations are required. Hence, the $p-d$ hybridization model cannot be excluded in this system. In such a sense, the ME behavior in $Ni_5(TeO_3)_4X_2$ is mainly attributed to the spin current mechanism. Of course, further investigation on the ME properties, including optical ME effect and neutron scattering on this system, deserves careful exploration.

IV. CONCLUSION

In conclusion, we have presented direct observation of linear magnetoelectric effect in the van der Waals antiferromagnet $Ni_5(TeO_3)_4X_2$ (X = Cl, Br). Here, we have carefully investigated the magnetism, specific heat, field-induced electric polarization, and magnetoelectricity of single crystal $Ni_5(TeO_3)_4X_2$ with a monoclinic lattice structure with a $C2/c$ space group. The field-driven electric polarization was observed in $Ni_5(TeO_3)_4X_2$ below T_{EF} ($\sim$29 K), implying that the intrinsic ME effect appears along with the formation of long-range spin order. Especially, the existence of off-diagonal ME coefficients in $Ni_5(TeO_3)_4X_2$ indicates the formation of ferrotoroidic order, which may give rise to intriguing phenomena related to the coupling between magnetic order, ferroelectricity, and dimension of materials in vdW magnets.

ACKNOWLEDGMENTS

This work was financially supported by the National Natural Science Foundation of China (Grants No. 92163210, No. 12274231, No. 11834002, No. 11947092, No. 51721001, No. 12074111, No. 12304124, and No. 11974167). We would also like to express our gratitude to Prof. W. Haihu from Nanjing University for their invaluable assistance with magnetic testing. In addition, we sincerely thank all the referee's comments and suggestions, which are very important and helpful for us to improve our work and its presentation.

[1] W. Eerenstein, N. D. Mathur, and J. F. Scott, Multiferroic and magnetoelectric materials, Nature (London) **442**, 759 (2006).

[2] S.-W. Cheong and M. Mostovoy, Multiferroics: A magnetic twist for ferroelectricity, Nat. Mater. **6**, 13 (2007).

[3] S. Dong, J.-M. Liu, S.-W. Cheong, and Z. F. Ren, Multiferroic materials and magnetoelectric physics: Symmetry, entanglement, excitation, and topology, Adv. Phys. **64**, 519 (2015).

[4] N. A. Spaldin and R. Ramesh, Advances in magnetoelectric multiferroics, Nat. Mater. **18**, 203 (2019).

[5] T. Kosub, M. Kopte, R. Hühne, P. Appel, B. Shields, P. Maletinsky, R. Hübner, M. O. Liedke, J. Fassbender, O. G. Schmidt, and D. Makarov, Purely antiferromagnetic magnetoelectric random access memory, Nat. Commun. **8**, 13985 (2017).

[6] A. Iyama and T. Kimura, Magnetoelectric hysteresis loops in Cr_2O_3 at room temperature, Phys. Rev. B **87**, 180408(R) (2013).

[7] I. Kornev, M. Bichurin, J.-P. Rivera, S. Gentil, H. Schmid, A. G. M. Jansen, and P. Wyder, Magnetoelectric properties of $LiCoPO_4$ and $LiNiPO_4$, Phys. Rev. B **62**, 12247 (2000).

[8] K. Yoo, B. Koteswararao, J. Kang, A. Shahee, W. Nam, F. F. Balakirev, V. S. Zapf, N. Harrison, A. Guda, N. Ter-Oganessian, and K. H. Kim, Magnetic field-induced ferroelectricity in $S = 1/2$ kagome staircase compound $PbCu_3TeO_7$, npj Quantum Mater. **3**, 45 (2018).

[9] T. Kurumaji, S. Ishiwata, and Y. Tokura, Doping-Tunable ferrimagnetic phase with large linear magnetoelectric effect in a polar magnet $Fe_2Mo_3O_8$, Phys. Rev. X **5**, 031034 (2015).

[10] K. S. Burch, D. Mandrus, and J.-G. Park, Magnetism in two-dimensional van der Waals materials, Nature (London) **563**, 47 (2018).

[11] C. Gong and X. Zhang, Two-dimensional magnetic crystals and emergent heterostructure devices, Science **363**, eaav4450 (2019).

[12] M. Gibertini, M. Koperski, A. F. Morpurgo, and K. S. Novoselov, Magnetic 2D materials and heterostructures, Nat. Nanotechnol. **14**, 408 (2019).

[13] S. X. Yang, T. L. Zhang, and C. B. Jiang, van der Waals Magnets: Materials family, detection and modulation of magnetism, and perspective in spintronics, Adv. Sci. **8**, 2002488 (2021).

[14] D. R. Klein, D. Macneill, J. L. Lado, D. Soriano, E. Navarro-Moratalla, K. Watanabe, T. Taniguchi, S. Manni, P. Canfield, J. Fernández-Rossier, and P. Jarillo-Herrero, Probing magnetism in 2D van der Waals crystalline insulators via electron tunneling, Science **360**, 1218 (2018).

[15] S. W. Jiang, J. Shan, and K. F. Mak, Electric-filed switching of two-dimensional van der Waals magnets, Nat. Mater. **17**, 406 (2018).

[16] X. L. Wang, Z. X. Shang, C. Zhang, J. Q. Kang, T. Liu, X. Y. Wang, S. L. Chen, H. L. Liu, W. Tang, Y.-J. Zeng, J. F. Guo, Z. H. Cheng, L. Liu, D. Pan, S. C. Tong, B. Wu, Y. Y. Xie, G. C. Wang, J. X. Deng, T. R. Zhai *et al.*, Electrical and magnetic anisotropies in van der Waals multiferroic $CuCrP_2S_6$, Nat. Commun. **14**, 840 (2023).

[17] A. Koitzsch, T. Klaproth, S. Selter, Y. Shemerliuk, S. Aswartham, O. Janson, B. Büchner, and M. Knupfer, Intertwined electronic and magnetic structure of the van-der-Waals antiferromagnet $Fe_2P_2S_6$, npj Quantum Mater. **8**, 27 (2023).

[18] C. B. Park, A. Shahee, K.-T. Kim, D. R. Patill, S. A. Guda, N. Ter-Oganessian, and K. H. Kim, Observation of spin-induced ferroelectricity in a layered van der Waals antiferromagnet $CuCrP_2S_6$, Adv. Electron. Mater. **8**, 2101072 (2022).

[19] S. Zhang, X. Li, H. Zhang, P. Cui, X. Xu, and Z. Zhang, Giant Dzyaloshinskii-Moriya interaction, strong XXZ-type biquadratic coupling, and bimeronic excitations in the two-dimensional $CrMnI_6$ magnet, npj Quantum Mater. **8**, 38 (2023).

[20] M. Pregelj, A. Zorko, H. Berger, H. Van Tol, L. C. Brunel, A. Ozarowski, S. Nellutla, Z. Jagličič, O. Zaharko, P. Tregenna-Piggott, and D. Arcon, Magnetic structure of the $S = 1$ $Ni_5(TeO_3)_4Br_2$ layered system governed by magnetic anisotropy, Phys. Rev. B **76**, 144408 (2007).

[21] M. Johnsson, K. W. Törnroos, P. Lemmens, and P. Millet, Crystal structure and magnetic properties of a new Two-Dimensional $S = 1$ quantum spin system $Ni_5(TeO_3)_4X_2$ (X = Cl, Br), Chem. Mater. **15**, 68 (2003).

[22] Y. S. Oh, S. Artyukhin, J. J. Yang, V. Zapf, J. W. Kim, D. Vanderbilt, and S.-W. Cheong, Non-hysteretic colossal magnetoelectricity in a collinear antiferromagnet, Nat. Commun. **5**, 3201 (2014).

[23] X. Y. Wang, F.-T. Huang, J. J. Yang, Y. S. Oh, and S.-W. Cheong, Interlocked chiral/polar domain walls and large optical rotation in Ni_3TeO_6, APL Mater. **3**, 076105 (2015).

[24] Y. F. Lai, Z. G. Song, Y. Wan, M. Z. Xue, C. S. Wang, Y. Ye, L. Dai, Z. D. Zhang, W. Y. Yang, H. L. Du, and J. B. Yang, Two-dimensional ferromagnetism and driven ferroelectricity in van der Waals $CuCrP_2S_6$, Nanoscale **11**, 5163 (2019).

[25] Y. Tokunaga, D. Okuyama, T. Kurumaji, T. Arima, H. Nakao, Y. Murakami, Y. Taguchi, and Y. Tokura, Multiferroicity in $NiBr_2$ with long-wavelength cycloidal spin structure on a triangular lattice, Phys. Rev. B **84**, 060406(R) (2011).

[26] P. Tolédano, A. P. Ayala, A. F. G. Furtado Filho, J. P. C. do Nascimento, M. A. S. Silva, and A. S. B. Sombra, Magnetoelectric effects in the spiral magnets $CuCl_2$ and $CuBr_2$, J. Phys.: Condens. Matter **29**, 035701 (2017).

[27] T. Kurumaji, S. Seki, S. Ishiwata, H. Murakawa, Y. Tokunaga, Y. Kaneko, and Y. Tokura, Magnetic-field induced competition of two multiferroic orders in a triangular-lattice helimagnet MnI_2, Phys. Rev. Lett. **106**, 167206 (2011).

[28] T. Kurumaji, S. Seki, S. Ishiwata, H. Murakawa, Y. Kaneko, and Y. Tokura, Magnetoelectric responses induced by domain rearrangement and spin structural change in triangular-lattice helimagnets NiI_2 and CoI_2, Phys. Rev. B **87**, 014429 (2013).

[29] Y. Tokura, S. Seki, and N. Nagaosa, Multiferroics of spin origin, Rep. Prog. Phys. **77**, 076501 (2014).

[30] K. Momma and F. Izumi, Vesta 3 for three-dimensional visualization of crystal, volumetric and morphology data, J. Appl. Crystallogr. **44**, 1272 (2011).

[31] G. Kresse and J. Furthmuller, Efficiency of *ab-initio* total energy calculations for metals and semiconductors using a plane-wave basis set, Comput. Mater. Sci. **6**, 15 (1996).

[32] G. Kresse and D. Joubert, From ultrasoft pseudopotentials to the projector augmented-wave method, Phys. Rev. B **59**, 1758 (1999).

[33] J. P. Perdew, K. Burke, and M. Ernzerhof, Generalized gradient approximation made simple, Phys. Rev. Lett. **77**, 3865 (1996).

[34] Jesse Kapeghian and Antia S. Botana, Electronic structure and magnetism in infinite-layer nickelates $RNiO_2 (R = \mathrm{La} - \mathrm{Lu})$, Phys. Rev. B **102**, 205130 (2020).

[35] A. Tari, *The Specific Heat of Matter at Low Temperatures* (Imperial College Press, London, 2003).

[36] Y. S. Tang, S. M. Wang, L. Lin, C. Li, S. H. Zheng, C. F. Li, J. H. Zhang, Z. B. Yan, X. P. Jiang, and J.-M. Liu, Collinear magnetic structure and multiferroicity in the polar magnet $Co_2Mo_3O_8$, Phys. Rev. B **100**, 134112 (2019).

[37] F. Xue, Y. Hou, Z. Wang, and R. Wu, Two-dimensional ferromagnetic van der Waals $CrCl_3$ monolayer with enhanced anisotropy and Curie temperature, Phys. Rev. B **100**, 224429 (2019).

[38] R. Jana, D. Sheptyakov, X. Y. Ma, J. A. Alonso, M. C. Pi, A. Muñoz, Z. Y. Liu, L. L. Zhao, N. Su, S. F. Jin, X. B. Ma, K. Sun, D. F. Chen, S. Dong, Y. S. Chai, S. L. Li, and J. G. Cheng, Low-temperature crystal and magnetic structures of the magnetoelectric material $Fe_4Nb_2O_9$, Phys. Rev. B **100**, 094109 (2019).

[39] N. D. Khanh, N. Abe, H. Sagayama, A. Nakao, T. Hanashima, R. Kiyanagi, Y. Tokunaga, and T. Arima, Magnetoelectric coupling in the honeycomb antiferromagnet $Co_4Nb_2O_9$, Phys. Rev. B **93**, 075117 (2016).

[40] L. Lin, Y. S. Tang, L. Huang, W. J. Zhai, G. Z. Zhou, J. H. Zhang, M. F. Liu, G. Y. Li, X. Y. Li, Z. B. Yan, and J. -M. Liu, Observation of magnetoelectric effect in the $S = 1/2$ spin chain compound $CoSe_2O_5$ single crystal, Appl. Phys. Lett. **120**, 052901 (2022).

[41] V. Kocsis, Y. Tokunaga, Y. Tokura, and Y. Taguchi, Switching of antiferromagnetic states in $LiCoPO_4$ as investigated via the magnetoelectric effect, Phys. Rev. B **104**, 054426 (2021).

[42] V. Kocsis, T. Nakajima, M. Matsuda, A. Kikkawa, Y. Kaneko, J. Takashima, K. Kakurai, T. Arima, Y. Tokunaga, Y. Tokura, and Y. Taguchi, Stability of multiferroic phase and magnetization-polarization coupling in Y-type hexaferrite crystals, Phys. Rev. B **101**, 075136 (2020).

[43] B. B. Van Aken, J.-P. Rivera, H. Schmid, and M. Fiebig, Observation of ferrotoroidic domains, Nature (London) **449**, 702 (2007).

[44] J.-P. Rivera, On definitions, units, measurements, tensor forms of the liner magnetoelectric effect and on a new dynamic method applied to Cr-Cl boracite, Ferroelectrics **161**, 165 (1994).

[45] S. Toyoda, N. Abe, S. Kimura, Y. H. Matsuda, T. Nomura, A. Ikeda, S. Takeyama, and T. Arima, One-Way transparency of light in multiferroic CuB_2O_4, Phys. Rev. Lett. **115**, 267207 (2015).

[46] G. T. Rado, Statistical theory of magnetoelectric effects in antiferromagnetics, Phys. Rev. **128**, 2546 (1962).

[47] R. Hornreich and S. Shtrikman, Statistical mechanics and origin of the magnetoelectric effect in Cr_2O_3, Phys. Rev. **161**, 506 (1967).

[48] G. A. Gehring, On the microscopic theory of the magnetoelectric effect, Ferroelectrics **161**, 275 (1994).

[49] M. Mostovoy, A. Scaramucci, N. A. Spaldin, and K. T. Delaney, Temperature-Dependent magnetoelectric effect from first principles, Phys. Rev. Lett. **105**, 087202 (2010).

[50] H. Katsura, N. Nagaosa, and A. V. Balatsky, Spin current and magnetoelectric effect in noncollinear magnets, Phys. Rev. Lett. **95**, 057205 (2005).

[51] I. A. Sergienko, C. Sen, and E. Dagotto, Ferroelectricity in the magnetic E-phase of orthorhombic perovskites, Phys. Rev. Lett. **97**, 227204 (2006).

[52] T. Arima, Ferroelectricity induced by proper-screw type magnetic order, J. Phys. Soc. Jpn. **76**, 073702 (2007).